A neural progenitor mitotic wave is required for asynchronous axon outgrowth and morphology

Jérôme Lacoste[1*], Hédi Soula[2], Angélique Burg[1], Agnès Audibert[1], Pénélope Darnat[1], Michel Gho[1#*] and Sophie Louvet-Vallée[1#*]

[1] Sorbonne Université, CNRS, Laboratoire de Biologie du Développement - Institut de Biologie Paris Seine (LBD-IBPS), Cell cycle and cell determination Team, F-75005 Paris, France.

[2] Sorbonne Université, INSERM, NutriOmics Research Unit Paris, F-75013, France.

Key Words: mitotic wave; sensory organ progenitor/precursor; neurogenesis; peripheral and central nervous system; axon branching; behavior; *Drosophila*; Scabrous; filopodia.

co-last authors

* authors for correspondence: jerome.lacoste@sorbonne-universite.fr; michel.gho@sorbonne-universite.fr; sophie.louvet_vallee@sorbonne-universite.fr

SUMMARY

Spatiotemporal mechanisms generating neural diversity are fundamental for understanding neural processes. Here, we investigated how neural connection diversity arises from neurons coming from identical progenitors. In the dorsal thorax of *Drosophila*, rows of mechanosensory organs originate from the division of sensory organ progenitor (SOPs). We show that in each row of the notum, a central SOP divides first, then neighboring SOPs divide, and so on. This centrifugal wave of mitoses depends on cell-cell inhibitory interactions mediated by SOP cytoplasmic protrusions and Scabrous, a secreted protein interacting with the Delta/Notch complex. When *scabrous* was downregulated, the mitotic wave was abolished, axonal growth was more synchronous, axonal terminals had a complex branching pattern and fly behavior was impaired. We propose that the temporal order of progenitor divisions influences the birth order of sensory neurons which is critical for correct axon wiring and appropriate grooming behavior, supporting the idea that developmental timing controls neural connectivity.

INTRODUCTION

It is commonly accepted that nervous system development relies on the precise spatio-temporal regulation of gene expression in neural progenitors (Holguera and Desplan, 2018). However, little is known about how neural diversity can be generated among neural progenitors that are homogenously specified (Hirata and Iwai, 2019), for example, in neurons that connect peripheral sensory organs with the central nervous system (Gatto et al., 2019).

Microchætes are peripheral mechanosensory organs on the thorax of *Drosophila melanogaster*. These organs arise from sensory organ progenitor cells (SOPs) which are selected among G2 arrested cells of proneural clusters during pupal stage (Sato et al., 1999; Usui and Kimura, 1993). In the dorsal region of the thorax (notum), SOPs appear sequentially from five parallel proneural rows: first rows 1 and 5, followed by row 3 and finally rows 2 and 4 (Usui and Kimura 1993, Simpson 1999). SOP selection involves Notch-dependent lateral inhibition as well as modulators, such as Scabrous (Sca), from 6 to 12 h after pupal formation (APF). Then, at 16.5 h APF, SOPs resume the cell cycle and undergo a sequence of divisions to generate a neuron and three other non-neural support cells (the shaft, the sheath and the socket cells) to form each organ (Gho et al., 1999). During organogenesis, the bipolar neurons project their dendrite toward the base of the bristle, and their axons toward the ventral thoracic ganglion. The axons enter the ganglion through the posterior dorsal mesothoracic nerve root and extend branches anteriorly and posteriorly (Ghysen, 1980). The resulting arborization of the microchæte axon projections is variable. Their complexity is not correlated to the position of the organ but to the time at which rows appear (Ghysen, 1980; Usui-Ishihara and Simpson, 2005). Thus, the earlier the microchaetes developed, wherever they were positioned, the more branched they were, arborizing over a greater area within the neuropil.

In adult flies, mechanical stimulation of thoracic bristles requires the correct connectivity of the bristle neurons, to induce the cleaning reflex of sweeping the stimulated area with the first or third leg (Corfas and Dudai, 1989; Ghysen, 1980). When flies are covered with dust, all body bristles are activated inducing a grooming response. Grooming is a hierarchical stereotyped sequence progressing from anterior to posterior to remove dust (Phillis et al., 1993; Zhang et al., 2020).

In this model system, we investigated how resumption of SOP division within the notum influences neurogenesis and ultimately fly behavior. In a kinetic study, we show that SOP cells enter mitosis successively according to a temporal wave that propagates from the center towards the anterior and the posterior border of the thorax. We took a genetic approach to demonstrate that the Notch-ligand Delta and the secreted Notch-signaling modulator Scabrous control this wave. By altering cellular morphology, we show that propagation of the wave is mediated by cell-cell interactions through cell protrusions from SOPs. Finally, we present evidence showing that this mitotic wave has an impact on neural wiring and grooming behavior. Overall, our data support the idea that timing of neural progenitor divisions controls normal wiring in the central nervous system.

RESULTS

SOP mitosis resumes in a temporal wave

To monitor mitosis in SOPs, transgenic pupae at 15h APF expressing GFP under the SOP specific *neuralized* driver (*neurD::GFP)* were monitored with live imaging. As a way to comparing nota, the first cell in each row to divide was used as both a temporal (division time, min) and a positional reference (rank, µm), designated SOP_o. Centering our attention on SOPs located in the dorsal most region of the thorax (Rows 1-3 in Fig 1A), we observed that the SOP_o cells were located in the medial region of each row and generally, the more distant a SOP was from its corresponding SOP_o, the later it divided (Fig 1A-B). The order of mitosis of SOPs was not strict. However, plotting the time of SOP division against its rank relative to SOP_o, reveals that on average SOPs resumed the cell cycle in a wave of mitoses spreading towards the anterior and the posterior ends along each row. Thus, all SOPs in a row divided in two hours for all rows analyzed (Fig 1B, 1C and S1A). No statistical difference was found between the rate of the mitotic waves in rows 1, 2 and 3 ($p = 0.3954$, ANOVA) or between left and right rows ($p = 0.3038$, ANOVA). SOP_o were not located precisely in the middle of each row, so the number of SOPs in the anterior and posterior portion of each row was unequal (Fig 2A-C and S1). Still, no statistical difference was found between the rates of the anterior and posterior mitotic waves ($p = 0.0689$, ANOVA). The rate of the mitotic wave was calculated as the mean absolute value of the inverse of the slopes of the curves for all rows, giving 3.14 µm min^{-1} (see Table S1). We conclude that the resumption of SOP mitosis is not random because the first division is in a specific region of the notum and a steady wave of division propagates towards the anterior and the posterior parts of the notum.

To establish working hypotheses on the mechanism involved in the propagation of this mitotic wave, we pooled all the data and modelled the resulting mitotic wave. A simple contagion model accounts for the observed propagation of SOP mitoses very well (Fig 1D and see key resource table). In the chosen model,

we assumed that (1) neighboring progenitor cells in a row inhibit each other from entering mitosis through cell-cell contact, (2) this inhibition is switched off when cells divide, (3) mitoses occur whenever a cellular compound concentration reaches a certain threshold and (4) this compound is produced at a constant rate.

Long cytoplasmic protrusions are required for the SOP mitotic wave

Based on this model, SOPs are likely to influence neighboring SOPs, so we analyzed the potential ways by which they interact. SOPs in each row are actually separated by 3-4 epithelial cells, but SOPs produce dynamic actin-based protrusions several cell diameters in length that physically interact with protrusions from neighboring SOPs and epithelial cells (Cohen et al., 2010; Hunter et al., 2016; Renaud and Simpson, 2001) (Fig 3A left). When SOPs divide, they become spherical and protrusions are drastically reduced. To test the possibility that these protrusions control the mitotic wave, we overexpressed a dominant negative form of Rac1 (*rac1*^{N17}) (Fig 3A right), because Rac1 is required for the growth of protrusions in SOPs (Cohen et al., 2010). Under these conditions, SOP protrusions were shorter than in the control (Fig 3B, p = 0.0009, ANOVA). Although SOP divisions started at similar developmental times (control 15.7 ± 0.5 h APF, n = 9; *rac1*^{N17} overexpression 15.9 ± 0.5 h APF, n = 6), we observed that SOPs with shorter protrusions divide more synchronously than in the control (Fig 3C, mitotic wave rate 6.95 µm min^{-1}). Indeed, all SOPs in a row divided within one hour for all rows analyzed (Fig 3C, Row 1 $p < 0.0001$; Row 2 $p = 0.0292$, Row 3 $p = 0.0014$, ANOVA, and Fig S2). The lesser slopes of the time-rank curves of the mitotic wave in flies with short SOP protrusions shows that neighboring SOPs resume mitosis earlier than normal. We can hypothesize that SOPs exchange inhibitory signals throughout protrusions to maintain neighboring SOPs in G2-arrest. When a SOP divides, its protrusions are retracted so the inhibitory signal is suppressed allowing progression of the mitotic wave to the next SOP along the row.

The SOP mitotic wave is regulated by Scabrous and Delta

Cellular protrusions allow molecules to be exchanged between cells for direct and selective signaling (Buszczak et al., 2016; Kornberg and Roy, 2014). The candidate for such a signal would be a secreted molecule with a role in regulating the interactions and spacing of cells in the nervous system. One such molecule is the fibrinogen-like protein Scabrous (Sca) that regulates several processes such as the regularly spaced pattern of ommatidia in the eye or of bristles in the notum (Baker et al., 1990; Cohen et al., 2010; Gavish et al., 2016; Renaud and Simpson, 2001), or ommatidial rotation (Chou and Chien, 2002). In the protein trap line *sca::GFP*, Sca was detected as multiple spots of fluorescence in the cytoplasm and along the protrusions of SOPs (Fig 3D). To investigate whether Sca is involved in the synchronization of SOP mitosis, we studied the mitotic wave in the *sca*^{BP2} null mutant, which is viable at the developmental period studied. In this mutant, we observed SOP$_o$ cells at different points along each row as they were not limited to the anterior region (Fig 2B-C and S1B). More importantly, in the *sca*^{BP2} mutant, SOPs divided more simultaneously than in the control (Row 1, $p = 0.0015$; Row 2, $p = 0.0029$; Row 3, $p = 0.0014$, ANOVA, Fig 4A-B, Figs S1, S3A). For instance, Row 1 in *sca*^{BP2} divided in one-third of time taken for the control SOP row to divide, and the rate of the wave increased to 20.27 µm min^{1} (Table S1). This effect is not likely

to be related to protrusion length shortening because no difference was found between *sca*^{BP2} and control SOP protrusions (Renaud and Simpson, 2001). To exclude the possibility that the absence of Sca during the development of *sca*^{BP2} mutant could secondarily impact the mitotic wave, *sca* expression was specifically downregulated using a conditional RNAi strategy between 12 and 19 h APF (Fig S3B), that is from just before and during the mitotic wave. The kinetics of the SOP mitotic wave in the downregulated conditions was similar to that in the null mutant (Fig S3C; Row 1, $p < 0.0001$; Row 2, $p = 0.69$; Row 3, $p = 0.003$, ANOVA; Fig S2). These data indicate that Sca transported through cell protrusions specifically controls the wave of SOP mitoses along the rows.

Sca is known to modulate the Delta/Notch (Dl/N) pathway (Petruccelli et al., 2018), so we tested whether this pathway is involved in regulating the SOP mitotic wave. Null *Dl* mutants are lethal, so we studied this allele in the *Dl*^{7}/+ heterozygous line. We did not observe a statistically significant reduction in the mitotic wave rate in *Dl*^{7}/+ SOPs (Fig 4C, $p = 0.69$, ANOVA). Similarly, we did not observe any difference in the rate of the SOP division wave in the *sca*^{BP2}/+ heterozygous line (Fig 4D, $p = 0.71$, ANOVA). By contrast, when the gene dosage of both *sca* and *Dl* was reduced by half, the time-rank curves were flattened corresponding to a significant increase in the mitotic wave rate (from 3.14 to 43.35 µm min^{-}1) (Fig 4E, $p = 0.048$, ANOVA). These results demonstrate that *sca* and *Dl* genetically interact, which suggests that these factors act in concert to control the SOP mitotic wave. Indeed, we observed that Dl and Sca co-localize in vesicle-like structures inside the cytoplasm with Dl surrounding the Sca aggregates (Fig 4F). This co-localization firstly described Renaud and Simpson (2001), evidences that these two proteins are transported from the endoplasmic reticulum to the membrane in the same vesicles.

Altogether, our results show that the wave of SOP mitoses along rows depends on an inhibitory signal transmitted by protrusions from the progenitors and is controlled by Dl and Sca proteins.

Outcome of the mitotic wave on microchæte axonogenesis

Considering the invariability of sensory organ formation, we wondered whether differences in the wave of SOP mitosis might impact the timing of axonogenesis along each row. To this end, we measured axon length at the beginning of axonogenesis (24 h APF) in control and *sca*^{BP2} pupae (Fig 5A). In control pupae, the axon length varied along the antero-posterior axis. Indeed, within a row, more the neurons were located at the extremities, the shorter their own axon. However, in *sca*^{BP2} animals, the length of the axon along a row was significantly more homogeneous (Fig 5B, $p = 0.0232$, ANOVA). These observations indicate that as a result of the SOP mitotic wave, neurogenesis and consequently axonogenesis progress from the centrally located neurons towards those located at the extremities in controls, while in *sca* mutants, in which the wave was either reduced or absent, axonogenesis occurs simultaneously along each row. Thus, the mitotic wave of SOP division controls axonogenesis timing.

Loss of the SOP mitotic wave leads to a modified organization of microchæte axonal projections.

We wondered whether the altered axonogenesis timing observed in the mutant bristle organs influences the patterning of axonal endings in the thoracic ganglion. To address this question, the morphology of these

axon terminals was studied by expressing a membrane-bound GFP form in bristle cells using pannier-GAL4, as a driver of dorsal expression. Under these conditions, the neuropile in the thoracic ganglion formed by axon terminals from all bristles of the central dorsal notum was visualized as a mesh-like triangular structure formed by an anterior arm at each left and right sides and a posterior commissure that cross the midline (Fig 5C1). In 11% of ganglia analyzed in control flies a second medial commissure was observed (Fig S4 arrow). Interestingly, in flies in which the mitotic wave was abolished after *sca* downregulation (*RNAi-sca*), this percentage increased to 34% (Fig S4, $p = 0.0002$, Fisher's exact test). These observations prompted us to analyze single axon terminals by immunodetecting individual axons using the stochastic labelling method MCFO (Nern et al., 2015). We observed in control flies that individual axon terminals have two main primary branches, an anterior branch that does not cross the midline and a posterior branch that crosses the midline (Fig 5C1 and C3 top panel). In *RNAi-sca* animals, we observed that axon terminals are more branched (Fig 5C3 bottom panel). The lengths of primary anterior and posterior branches, between the root and the first branch point (Fig 5C2), of *RNAi-sca* axons were significantly shorter than those of control axons (Fig 5D, $p < 0.0001$ and $p = 0.0001$ respectively, ANOVA). Since *sca* was inactivated specifically and only during the mitotic wave, the effects observed could not have been due to a possible effect of *sca* on axonogenesis itself. As primary branches were shorter when SOP division occurred simultaneously on the notum, the timing of axonogenesis is likely to be an important factor controlling axon connectivity. Interestingly, our data are in agreement with studies showing that axon terminals of bristles from rows that are formed earlier, are more branched than those from rows that develop later (Usui-Ishihara and Simpson, 2005). As such, our results suggest that the order of birth of neurons in a given row contributes to the future connectivity of these neurons.

Loss of the SOP mitotic wave leads to changes in fly behavior

Finally, we wondered whether modifications in axon branching after disruption of normal SOP mitosis led to behavioral changes. Two different assays were used to test the function of the mechanosensory system of flies in which *sca* was specifically downregulated during the SOP mitotic wave. First, we looked at the cleaning reflex which is a patterned set of leg movements elicited in a fly when its thoracic bristles receive tactile stimulation from a puff of air (Fig 6A) (Corfas and Dudai, 1989; Vandervorst and Ghysen, 1980). We found that the number of air puffs required to elicit a leg response was significantly higher in flies in which the SOP mitotic wave was impaired (Fig 6B, $p = 0.028$, ANOVA). Second, after applying dust to flies' bodies, we measured their grooming response to remove the debris (Fig 6C) (Phillis et al., 1993). We observed that the percentage of flies with a clean thorax was higher in flies in which the SOP mitotic wave was impaired (Fig 6D, $p = 0.001$, Fisher's exact test).

DISCUSSION

Here, we took advantage of the invariant way in which sensory organs are located on the dorsal epithelium of *Drosophila*. This spatial configuration greatly facilitated the recognition and analysis of a

distinct temporal wave of SOP mitosis. Asynchrony in mitotic reactivation timing has been described in *Drosophila* larva neuroblasts. This differential timing is related to two cell cycle arrests: one population of neuroblasts is arrested in G2 while another population is arrested in G0 (Otsuki and Brand, 2018). G2-arrested neuroblasts resume mitosis earlier than those in G0-arrest. As in our system, it has been proposed that this particular order of division ensures that neurons form appropriate functional wiring. It is relevant that other temporal processes controlling the wiring of peripheral receptors with the central nervous system have been described in the *Drosophila* eye, another highly organized structure (Fernandes et al., 2017). It is conceivable that these temporal patterning mechanisms of neurogenesis, to date identified only in organized tissues, could be more widespread.

Cleaning reflex and grooming are behaviors resulting from complex sensory-motor circuitries. Grooming is a sequence of highly stereotyped movements by which flies clean their body parts in a hierarchical order (Seeds et al., 2014; Zhang et al., 2020). It is remarkable that these fly behaviors were significantly affected by altering the timing of microchaete precursor division in the dorsal thorax. The cleaning reflex has been traditionally analyzed after stimulation of macrochaetes rather than microchaetes as in the present work. Macro- and microchaetes have different patterns of terminal axon arborization, so it is not clear how to interpret our results. In another respect, the notum is the body part with the lowest priority in the grooming sequence (Hampel et al., 2017). It was again unexpected that modifications in axon terminals of sensory organs located on the notum would impair this complex behavior. We show that the SOP mitotic wave leads to a progressive neurogenesis along each row of microchaetes. This, in turn, would likely induce a particular pattern of microchæte axon arrival in the thoracic ganglion required for the proper organization of the neuropila in the central nervous system. Although we have documented this progressive axonogenesis, we do not know the strict pattern of axon arrival into the ventral ganglion. It would depend on the order of birth of neurons, and on the geometry of axon projections that fasciculate to form the dorsal mesothoracic nerves in the ganglion. In any case, we show here that, when *sca* function was specifically downregulated during the SOP mitotic wave, axonogenesis occurs almost simultaneously in each row of microchaetes. This certainly impairs the pattern of axon arrival into the ganglion leading to ectopic axon branching and changes in fly behavior. It would be interesting to know whether these impairments are specifically due to neurogenesis occurring simultaneously. To test this, we need find a way to induce different patterns of SOP mitotic entry, for instance, a centripetal wave or a random order. If the observed effect is specifically due to the simultaneity, normal behavior would be expected to be associated with other patterns of SOP division.

We observed that the first SOP (SOP_0) to divide was always located in the anteromedial region of each row. This may reflect the existence of a pre-pattern that causes SOPs located in that region to start dividing earlier than the others. Although the anteromedial region corresponds approximately to the posterior limit of expression of the transcription factor BarH1 (Sato et al., 1999), no factors specifically expressed in this region have yet been identified. Alternatively, as the location of SOP_0 is modified when Sca function was impaired, an interesting possibility is that SOP_0 is selected by an emergent process related to cell-cell interaction in the epithelium, rather than by a passive pre-pattern that organizes the first events in the notum.

We present evidence indicating that the secreted glycoprotein Scabrous, which is known to interact with the N-pathway to promote neural patterning, controls the kinetics of SOP mitosis in the notum. In proneural clusters, cells that express high levels of Dl and Sca become SOPs, while surrounding epithelial cells activate the N-pathway to prevent acquisition of a neural fate (Muskavitch, 1994; Renaud and Simpson, 2001; Buffin and Gho, 2010). Although Sca interacts physically with N and Dl and modulates their activities (Mok et al., 2005), the precise mechanism by which Sca regulates them is unknown. In the notum, *sca* mutants have an excess of bristles, a phenocopy of *N* mutants, indicating that Sca positively modulates N-activity (Renaud and Simpson, 2001). In wing discs, ectopic expression of *sca* inhibits N-pathway by reducing the interactions with its ligands (Lee et al., 2000). In eye discs, some studies indicate that Sca promotes N activation in response to Dl (Li, 2003) and others show that expression of *sca* in receptor precursor cells reduces N-activity (Muñoz-Soriano et al., 2016; Powell et al., 2001). Thus, the mechanism by which Sca modulates N-activity seems to be tissue specific. In eye and notum systems, Sca modulates N-activity at a long range. Indeed, during eye development, Sca is expressed in intermediate clusters in the morphogenic furrow and transported posteriorly in vesicles through cellular protrusions to negatively control ommatidial cluster rotation (Chou and Chien, 2002). Similarly, in the notum, SOP protrusions extend beyond several adjacent epithelial cells in which Dl and Scabrous are detected (Renaud and Simpson, 2001), confirmed in this study. Our data show that shorter protrusions as well as loss of function of Dl or Sca make the mitotic wave more synchronous. Thus, we propose that Sca, transported through protrusions, is required to maintain SOPs in G2 arrest. As in neuroblasts, G2 arrest in SOP cells is due to the downregulation of the promitotic factor Cdc25/String. Thus, overexpression of *string* in SOPs induces a premature entry into mitosis (Ayeni et al., 2016), while overexpression of negative regulators, like Wee1, maintain these cells in arrest (Fichelson and Gho, 2004). Possibly Sca negatively regulates *string* expression, perhaps through the N-pathway that it is known to control the level of String (Deng et al., 2001; Krejčí et al., 2009). Alternatively, it has been recently shown that the insulin-pathway also regulates String level (Otsuki and Brand, 2018). Moreover, in muscle precursors, cell proliferation is induced by the insulin-mediated activation of the N-pathway (Aradhya et al., 2015). These observations raise the interesting possibility that, in our system, insulin activates the N-pathway and Sca modulates this activation. Further investigations will be required in order to identify the link between Scabrous, the N/Dl- and insulin-pathways in the resumption of mitosis in SOPs.

During nervous system development, the complex patterns of neuronal wiring are achieved through the interaction between neuronal cell surface receptors and their chemoattractive or repulsive ligands present in the environment (McCormick and Gupton, 2020). An essential condition for proper axon guidance is the competence of neurons to respond to these environmental clues. It is generally agreed that neuron competence depends on the specific expression of transcriptional factors regulating their identity (Petrovic and Hummel, 2008). We show here that the timing of neuron formation is also a factor controlling their terminal morphology. We propose that the SOP mitotic wave induces a particular pattern of arrival of microchæte axons in the thoracic ganglion. This pattern establishes a specific framework of guidance cues on which circuits will be built and ultimately influencing an organism's behavior. Our findings support the

idea that, in addition to genetic factors, neurogenic timing is a parameter of development in the mechanisms controlling neural connectivity.

Acknowledgments:

We thank Marie-Emilie Terret (CIRB, Paris, France) and Bassem Hassam (ICM, Paris, France) for critical and constructive comments on the manuscript. We thank Sophie Gournet for the illustration of the graphical abstract. We are grateful Julie Perrin and Chloé Jean Baptiste Simonne for their participation in the experiments presented respectively in figures S4 and 5C-D.

This work was funded by institutional support from the Centre National de la Recherche Scientifique (CNRS) and Sorbonne University.

Author contributions:

Conceptualization: J.L., M.G., S.L.V.; Methodology: H.S. J.L., A.A., M.G., S.L.V.; Formal analysis: J.L., H.S.; Investigation: J.L., P.D, A.A., M.G., S.L.V.; Resources: A.B; Writing Original Draft: J.L., M.G., S.L.V. Funding: M.G.

Competing interests: Authors declare no competing interests.

Figures

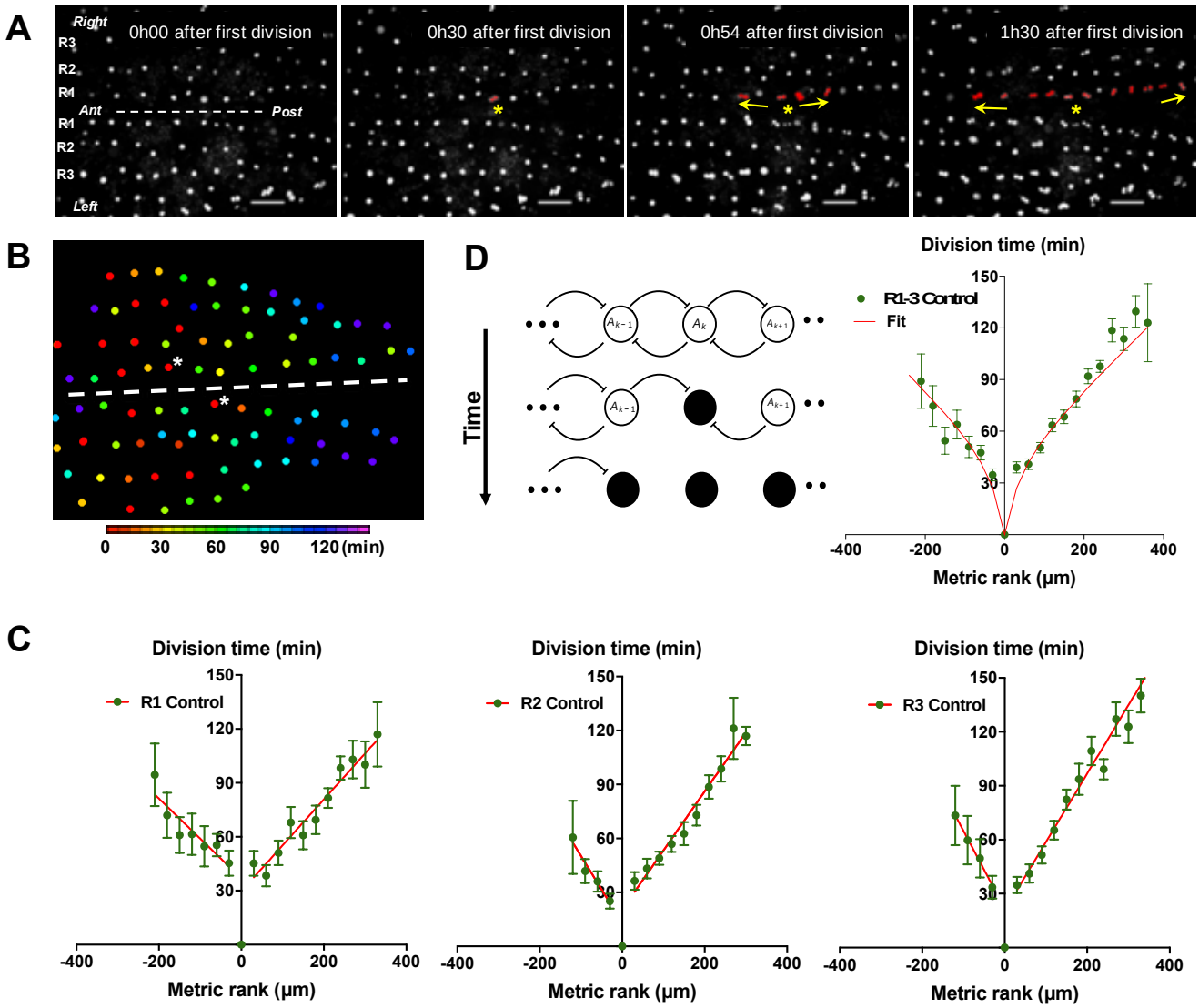

Figure 1. G2-arrested SOP cells of the neuroepithelium resume division in a temporal wave. (A) Four frames of a time-lapse recording of a control *Drosophila melanogaster* pupa. The first three rows of cells in the most dorsal part of the thorax are indicated as R1, R2 and R3 respectively. The dashed line marks the midline, with anterior (Ant) to the left and posterior (Post) to the right. SOPs that have divided are highlighted in red in R1. The yellow arrows indicate the propagation of the wave from SOP_0 marked by a yellow star. Scale bar, 50µm. (B) Heatmap of a representative control notum depicting time of SOP division. Circles represent SOP cells arranged in rows. The relative time of division is colour coded according to the scale, each colour covering 6 minutes. Only rows 1 to 4 are represented. The dashed line shows the midline, with anterior to the left, and SOP_0 in row 1 marked by white stars. (C) The time of SOP cell division (mean time ± SEM of n = 16 nota) in row 1 (R1), row 2 (R2) and row 3 (R3) is plotted according to position both relative to the position and time of division of the first cell to divide in each row. Negative and positive metric rank therefore corresponds to SOPs that are anterior and posterior to the SOP_0 respectively. Red lines show standard linear regressions. SOP cells were identified by GFP expression in a *neur-GFP* fly line. (D) Modelling the wave of SOP divisions. Left, a schematic view of the model at three consecutive times. Empty circles depict non-dividing cells. The flat-headed arrows indicate the inhibition that one cell exerts on immediate neighbours preventing entry into mitosis. Filled circles represent mitotic

or post-mitotic cells which no longer have an inhibitory effect thus allowing neighbours to divide. These interactions allow the progression of mitosis along a row. Right, fit of experimental data with theoretical values obtained with the model using as parameters ρ = 20 and μ = 0.65 (See Model in Supplementary material).

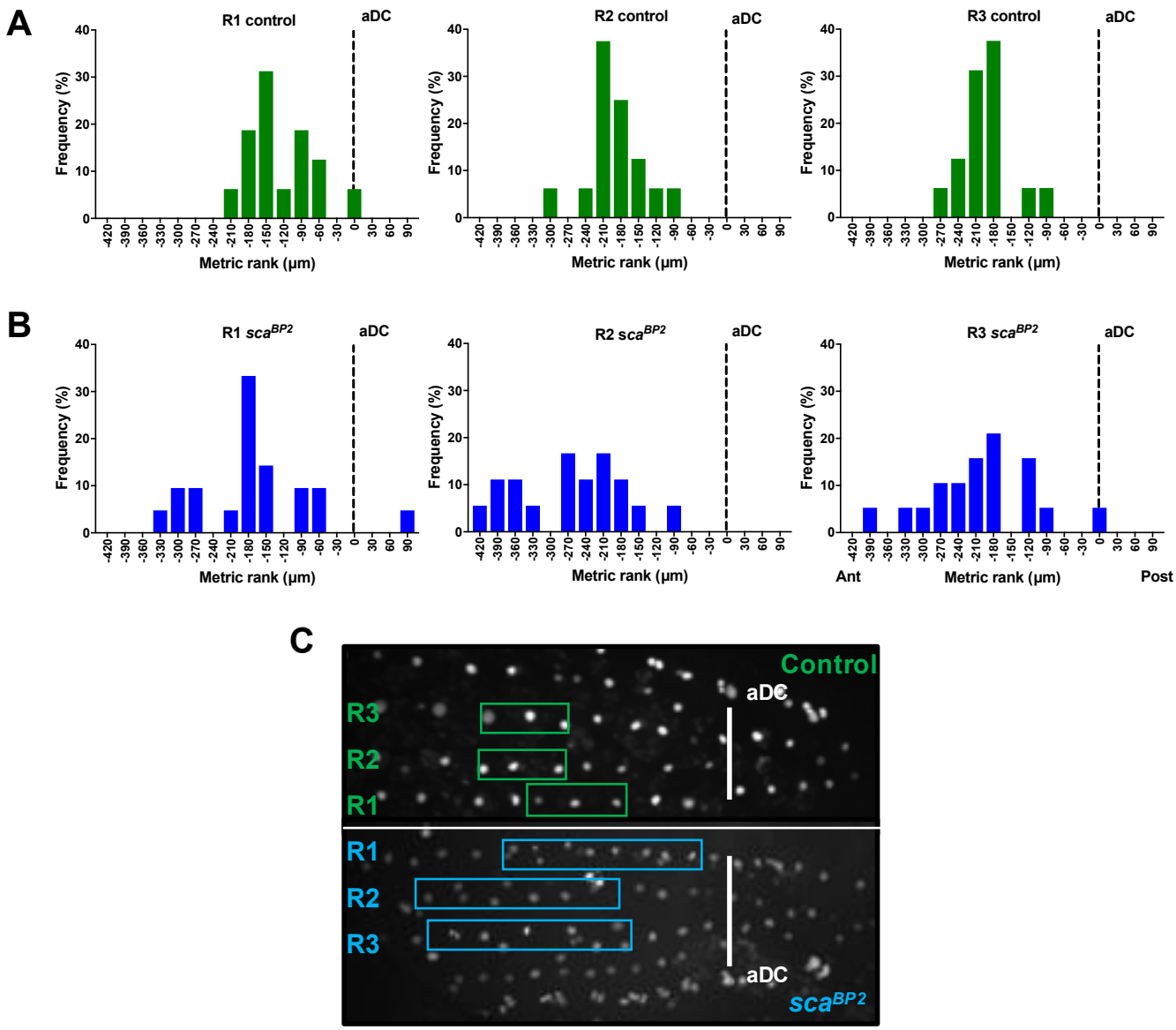

Figure 2. The mitotic wave origin spreads out in *sca* mutant.

Location of the first dividing SOP (SOP_0) in rows 1-3 in control flies (A) and sca^{BP2} flies (B). The line relaying the two antero-dorsocentral macrochætes (aDC) was used as a spatial reference (dotted line on graphs A and B) (see panel C). Negative and positive metric ranks correspond to SOPs anterior and posterior to the aDC line respectively. Graphs represent the frequency of SOP_0 at a given position recorded in 9 nota in row 1 (R1), row 2 (R2) and row 3 (R3). (C) Image of hemi-nota of a control fly and a sca^{BP2} homozygous mutant aligned anterior to the left showing the organisation of the SOPs in the notum. White vertical lines connecting the two aDC were used as spatial reference. Boxes show the locations of 68% of SOP_0 in each row, corresponding to one standard deviation from the mean.

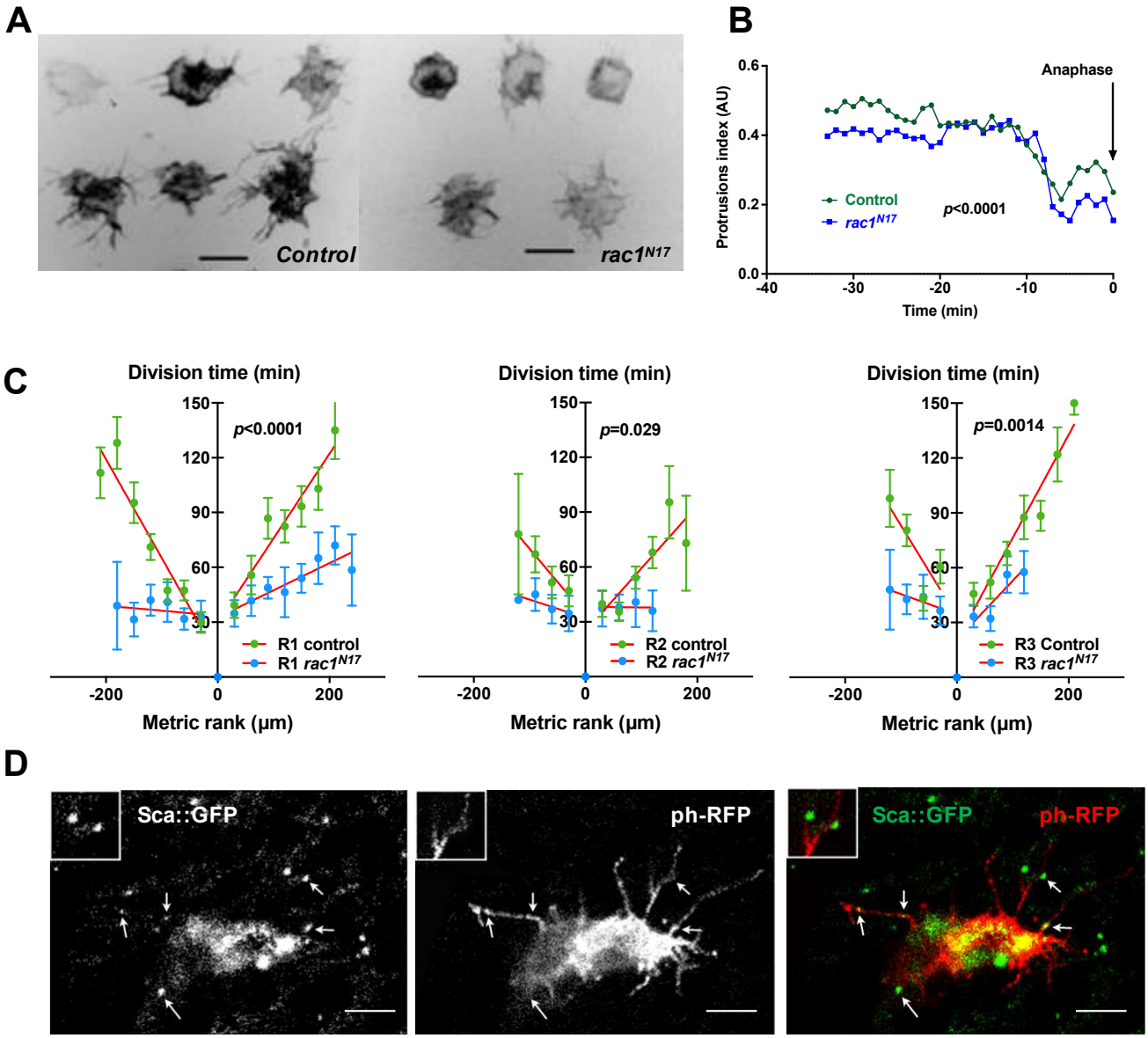

Figure 3. The SOP mitotic wave is controlled by signals exchanged via cell protrusions.

(A) Frames from live recordings showing cell protrusions of SOPs in control (left) and *rac1*^{N17} (right) pupae. Protrusions were visualized by specific expression of a membrane-tethered RFP form (*ph-RFP*), invert fluorescence. Scale bar, 20µm. (B) Relative protrusion length over time in control and after *rac1*^{N17} overexpression (mean ± SEM, n = 7 cells) measured from live recordings (see Methods). Anaphase was taken as a temporal reference. (C) The SOP mitotic wave in row 1 (R1), row 2 (R2) and row 3 (R3) in control and after overexpression of *rac1*^{N17}. Mean division time ± SEM of n = 6 nota. (D) Sca localisation in a SOP cell. Arrows indicate distinct Sca foci along cell protrusions. Scabrous (left panel) in SOP cell marked with a membrane bound ph-RFP (middle panel), merged in right panel. Images are a maximum projection of three confocal sections. Two Sca foci are magnified in the inserts. Scale bar, 5µm.

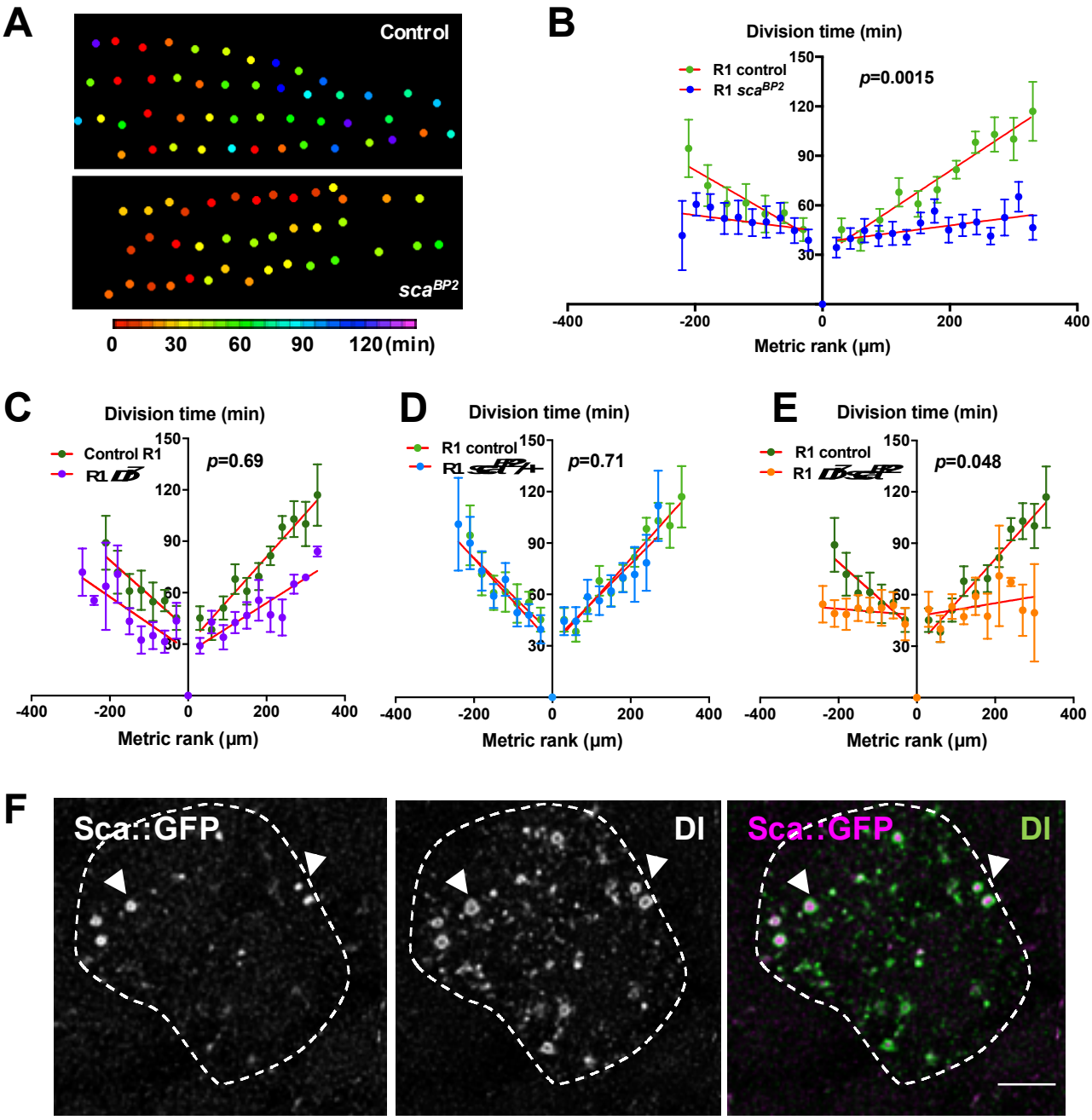

Figure 4. The mitotic wave of SOP cells is controlled by Notch/Delta/Scabrous signals.

(A) Heatmap of a representative heminota in control and *sca*^{BP2} homozygous null mutant aligned, anterior to the left. The relative time of SOPs division is colour coded according to the scale. (B) The SOP mitotic wave in row 1 in control and in *sca*^{BP2} homozygous mutant. (C-E) Genetic interactions between *Dl*^{7} and *sca*^{BP2}. Comparison of the SOP mitotic wave in control and *Dl*^{7} (C), *sca*^{BP2} (D) and *Dl*^{7}-*sca*^{BP2} (E). Mean division time ± SEM, n = 9, 8 and 11 nota respectively. (F) Confocal image of one SOP in a *sca::GFP* protein-trap fly at the moment of the SOP wave (16 h APF), immunostained for GFP (left panel) and Dl (middle panel), merged in the right panel (purple and green respectively). Arrowheads show co-localization of Dl and Sca into vesicle-like structures with Sca::GFP as puncta surrounded by Dl staining. SOP is delimitated by a dashed line. Scale bar, 5 µm.

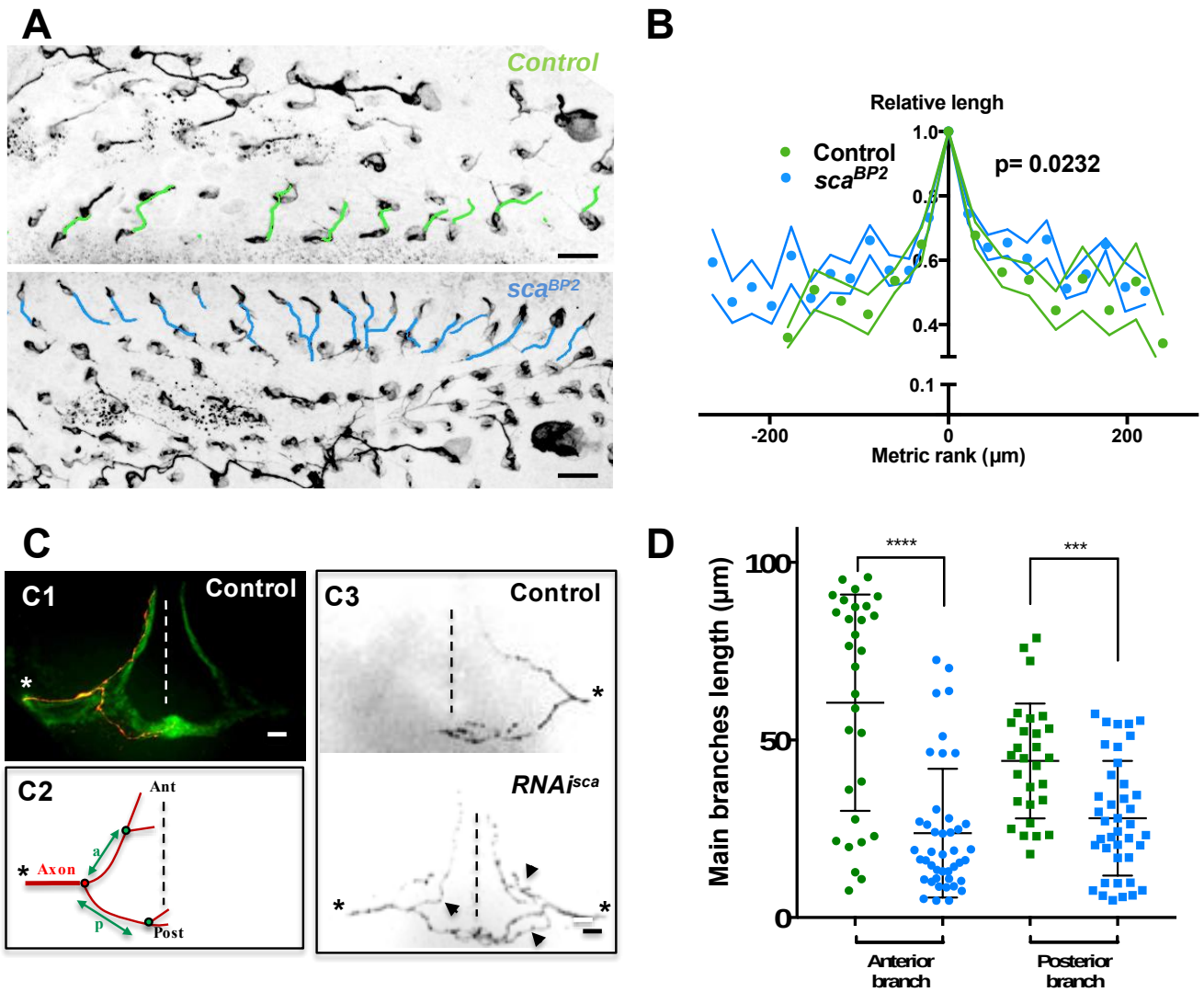

Figure 5. Microchæte axonal projections are affected by the amplitude of the SOP mitotic wave. (A) Axon immunostaining using anti-Futsch antibodies in control (w^{1118}) and sca^{BP2} heminota at 24h APF aligned, anterior to the left. Axons in row 1 were artificially coloured in green for w^{1118} and blue for sca^{BP2} homozygous flies. (B) Relative axon length of neurons belonging to sensory organs on row 1 plotted against relative position (mean length ± SEM of n = 18 rows). The neuron with the longest axon on the row was taken as temporal and spatial reference in control (w^{1118}) and sca^{BP2} homozygous pupae at 24h APF. (C) Axon projections of single sensory organ neurons in the thoracic ganglion identified with MCFO strategy. The midline is indicated by vertical dotted lines, anterior (Ant) up and posterior (Post) down. The asterisks indicate the point of entry of the sensory nerve into the thoracic ganglion. (C1) A single axon projection (red) counterstained with the neuropile formed by all axon terminals from sensory organs on the central notum (green). (C2) Schematic drawing of an axon projection. The length of the anterior (a) and posterior (p) primary branches were used to quantify the degree of branching of axon terminals. (C3) Representative examples of axon projections into the thoracic ganglion in control fly (top panel) and when the SOP mitotic wave was abolished (*RNAi-sca*) (bottom panel). Arrowheads point to additional branches in *RNAi-sca*. (D) Lengths of anterior and posterior primary branches in single axon terminals of control (green, n = 30) and in flies where the SOP mitotic wave was abolished (*RNAi-sca*) (blue, n = 43). Mean ± SEM ****$p < 0.0001$, ***$p = 0.0001$, two-tailed unpaired t-test.

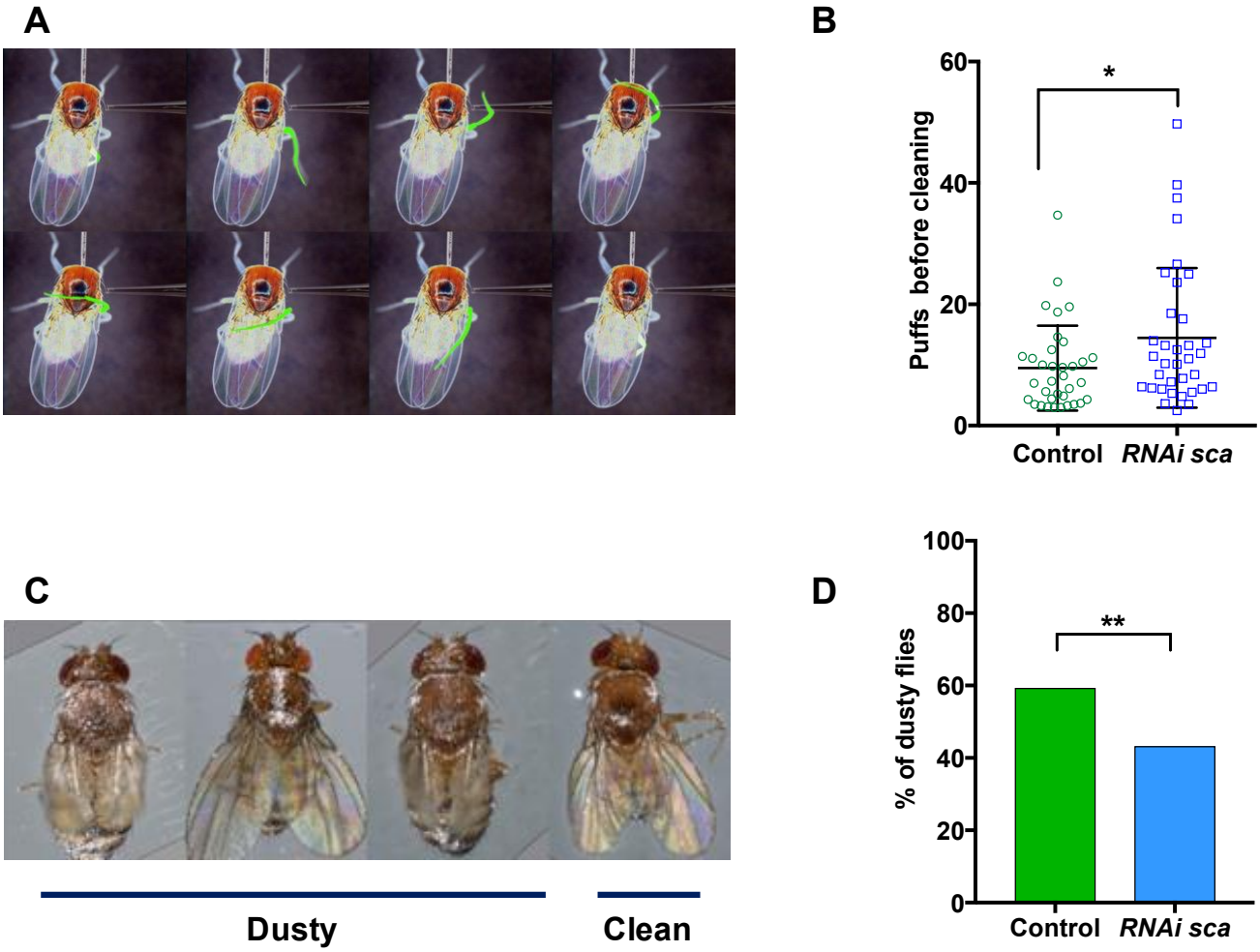

Figure 6. Loss of the SOP mitotic wave leads to changes in fly behavior

(A) Eight frames of a time-lapse recording of a decapitated control fly showing the sequence of movements upon stimulation of the dorsal bristles. (B) Number of air puffs required to elicit a cleaning reflex in control flies (n = 35) and in flies where the SOP wave was abolished (*RNAi-sca*) (n = 35). Mean ± SEM. *p = 0.0238; ANOVA. (C) Illustration of adult flies scored as dusty (left) and cleaned (right) observed 1 hour after shacked with talc. (D) Percent of dusty flies in control (green, n = 432) and when the SOP wave was abolished (blue, *RNAi-sca*, n = 394). **p = 0.001; Fisher's exact test.

METHODS

Fly strains

Standard methods were used to maintain fly stocks. The *Gal4/UAS* expression system was used to express several constructions in the mechanosensory bristle lineage as listed in the key resources table. Two drivers were used: *neuralized*^{p72}*>Gal4* (Bellaïche et al., 2001) expressed in SOPs and their descendants and *pannier>Gal4* (Sato and Saigo, 2000) expressed in the dorsal most domain all along pupal stage. For temporal control of transgene expression, *Gal4* drivers were combined with *tub-Gal80*^{ts}. Crossed flies, developing embryos and larvae were maintained at 18 °C and then pupae were shifted to 30 °C to allow the expression of *Gal4*. For the conditional inactivation of *sca*, the shift was done from 12 h APF to 19 h APF at the moment of the mitotic wave. To visualize SOP membranes specifically, we used a transgenic line expressing the pleckstrin homology domain of PLCδ fused to RFP (*ph-RFP*) under the control of the *neur* regulatory sequences (*neur-ph(PLCδ)-RFP*; gift of F. Schweisguth).

MultiColor FlipOut (MCFO) labelling

MCFO-1 flies (Nern et al., 2015) were crossed with *UAS-RNAi-sca, pnr-Gal4, tubGal*^{80ts}. For the control, the crosses were maintained at 18 °C until the progeny reached adulthood. For conditional inactivation of *sca*, pupae were shifted to 30 °C between 12 h APF to 19 h APF, then returned to 18 °C until they reached adulthood. In both cases, adults were heat-shocked at 37 °C for 12.5 min (to activate flipase expression), then left for two days at 25 °C to allow the expression of tags. After removing the head, the flies were fixed in 4% paraformaldehyde for 48 h and rinsed in T-PBS (0.1% Triton X100 in PBS). After dissection, thoracic ventral ganglions were incubated with primary antibodies overnight at 4 °C. After three T-PBS washes, ganglions were incubated with secondary antibodies for 1h at room temperature. Ganglions were mounted in Glycerol-PBS (80% glycerol in PBS) and imaged the same day.

Immunostaining

Dissected nota from pupae at 16 h APF for Scabrous detection or 24 h APF for axon labelling were processed as described previously (Gho et al., 1999). The antibodies used are described in the key resources (Table 2). Incubations with primary antibodies were done overnight at 4 °C and with the secondary antibodies for 1h at room temperature. Nota were mounted in Glycerol-PBS (80% glycerol in PBS, 1% propylgalate).

Confocal microscopy

Immunostaining was observed with an Olympus BX41 fluorescence microscope (objective 40X/1.30 or 63X/1.25) equipped with a Yokogawa spinning disc and a CoolSnapHQ2 camera driven by Metaview software (Universal Imaging).

For co-immunodetection of Scabrous and Delta, images were acquired with a Leica SP8 confocal microscope, with the HC PL APO CS2 93 X/1.30 GLYC objective. We tuned the white light laser (WLL)

to 650 nm for the excitation. The detector was a HyD. The pixel size was 0.087 µm and the z step size was 0.332 µm. Deconvolution was done with Huygens software. All images were processed with Fiji software (Schindelin et al., 2012).

Time-lapse recording

In vivo imaging was carried out as described previously (Gho et al., 1999). The temperature during the recording was controlled using a homemade Peltier device.

Image analysis

The division time of SOPs was analyzed for each row with Fiji. The first dividing SOP (SOP_0) provided the "zero time". For other SOPs, the timing of division was calculated according to this temporal reference. SOP_0 also defined the "rank zero". The rank of neighboring SOPs was incremented by one unit from this spatial reference. In order to compare several nota and take account for the neurogenic effect (the increase in the number of SOPs per row) observed in sca^{BP2}, we measured the distance between SOPs. In sca^{BP2}, the mean number of SOPs was 18 ± 3 separated by a distance of 22 ± 7.2 µm, while in other genetic backgrounds, there are 13 ± 1 SOPs separated by a distance of 30 ± 9 µm. For each graph, the metric rank corresponds to the rank multiplied by the mean distance between two SOPs.

Heatmaps

SOPs, identified using fly lines with the *neuralized* fluorescent construction, in pupae from 15 h APF were tracked by live imaging and the time of their division (identified as the anaphase mitotic figures) recorded. The position of cells at the moment of the division as well the relative time of division, encoded according to a rainbow scale, were used to construct each heatmap. The absolute time of division of the first cell which divides in each row was taken as temporal reference. In the dorsal thorax, no migration occurs, so cells keep the same neighbouring and cell positions were roughly those at the start of the live recordings.

Measurement of protrusion length

Live recording from *neur-ph(PLCδ)-RFP* pupae at 15 h APF were obtained by combining z-stacks (series of confocal optical sections separated by 1 µm) acquired every 3 min using a 40X oil immersion objective. Using a homemade ImageJ routine, records were made binary and a Protrusion Index was calculated as follows: Protrusion Index = [(Convex hull surface) - (Cell surface)] / [(Convex hull surface) (see below).

Cells presenting short or no protrusions have a Protrusion Index close to 0, while those presenting long protrusions have a Protrusion Index approximating 1.

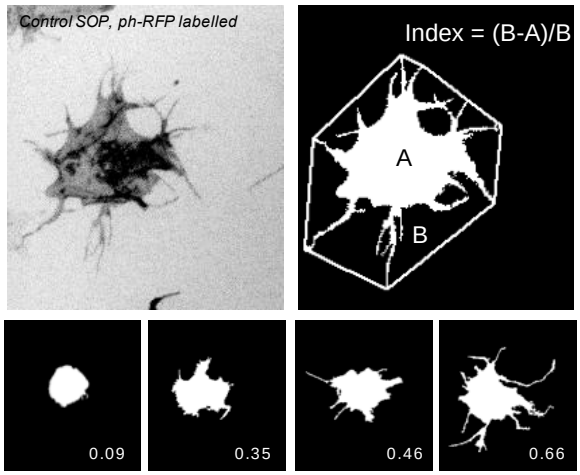

Left. Image of one SOP cell obtained from a frame of a time-lapse recording of a *ph-RFP* pupa. The image was obtained by combining a z-stack composed of optical sections (1 µm apart) through the entire cell, inverted fluorescence. Right. The same image as in left panel after binarization. The polygonal line corresponds to the convex closure of the image (convex hull). The index used to quantify protrusion length was defined as the area of the convex hull (B) minus the area of the cell (A) normalised to the area of the convex hull. Bottom. Examples of the index values in four SOPs. In cells devoid of protrusions this index was near zero, while the index is closer to 1 for cells presenting long protrusions.

Measurement of axon length

The length of axons in the nota and of the axon terminals in the thoracic ganglion was measured using the Simple Neurite Tracer plugin of Fiji. To compare the axon lengths of all the nota, the lengths were normalized to the longest axon in each row. The position of the neuron in each row was defined in the same as in the analysis of time of division. To estimate the extent of axon terminal branching in the thoracic ganglion, we measured the length of primary branches between the root and the first branch point (see Fig 4C2).

Cleaning reflex assay

Experiments were performed on headless flies. After decapitation, flies were allowed to recover for 1 h, then pasted at the tip of a Pasteur pipette. The most posterior thoracic bristles in the square formed by the four dorso-central macrochæte and the left dorso-central macrochæte were stimulated by air puffs from an Eppendorf microinjector. Specifically, a 0.1-second puff of 15 hPa was delivered every 0.5 second for a minute. For each fly, the stimulation was done 10 times. The number of puffs required to elicit the first leg movement was counted and the mean for each fly was calculated and plotted.

Grooming assay

Approximately 20 two-day-old flies were introduced into a plastic vial containing 150 mg of dry talc and shacked until they were totally covered. The flies were transferred to a plastic vial with a fine-mesh screen to remove the excess of talc. The flies were transferred to and shaken briefly in a third vial containing medium to remove any remaining unfixed talc. Then, the flies were transferred to an empty plastic vial

placed on its side for 1 h at room temperature. The flies were scored visually as clean when no talc particle remained on the notum, otherwise they were scored as dusty.

Statistics

For the mitotic wave study, all statistical analyzes were performed using statistical software R (r-project.org). To compare division time, Linear Mixed Models (LMM) were used. Normality of residuals and homoscedasticity were first assessed. Then LMM was performed using various variables. When a condition was found to be non-significantly different (e.g. Left or Right side of the notum) data were pooled but fly identification was maintained as a fix factor. For example, formula such as this one: lmer(TIME ~ COND + POS + ROW + (1|ID), data=data) was used to assess the impact of TIME according to POS (position) and COND (genetic condition in this example), corrected for ROW and for fly ID as a fixed factor. This test will yield significant influences of factors corrected by the others as well as *p*-values. Post-hoc analyzes were performed for the factor (e.g. ROW) only when the overall model was significant for this factor. For behavioural statistical tests, LMM was used to consider behavioural repetitions using fly ID as a fixed factor and the repetition number.

Unpaired *t* tests and Fisher's exact tests were done using Prism 7 software.

Model description

We use mathematical modelling techniques to understand wave propagation. In this model we make several assumptions: we first assume that (1) neighbouring progenitor cells are in a row and inhibit each other to enter into mitosis through cell contacts and (2) this inhibition is switched off when cells divide. We also assume that (3) cell division occurs whenever a certain cellular compound concentration (called A) reaches a certain threshold (θ). Finally, (4) this compound is produced at a constant rate but this production is inhibited (decreased) by direct neighbouring cells thus preventing the current cell from dividing.

Using dynamical systems, this can be modelled as (for a given cell indexed by k):

$$\rho \frac{dA_k}{dt} = \frac{r}{1+I_k} - A_k \qquad (1)$$

$$\delta \frac{dI_k}{dt} = \mu\,\mathrm{H}\left(A_{k+1}-\theta\right) + \mu\,\mathrm{H}\left(A_{k-1}-\theta\right) - I_k \qquad (2)$$

with

$$\mathrm{H}(x) = \begin{cases} 1 & x < 0 \\ 0 & x > 0 \end{cases}$$

As mentioned, A describes the compound concentration with constant production rate (r) inhibited by I another compound that decreases A's production rate. All degradations are at a constant rate (ρ and δ) as well. Inhibition is computed cell-wise and depends on neighbours' status. The production of inhibition is driven by μ. Higher values of μ indicate greater inhibition from neighbouring cells. Neighbouring cells

whose A is below the threshold (i.e that are not dividing) maintain the inhibition. Whenever the cell divides, inhibition vanishes. Please note that the extent of the inhibition is for direct neighbours only hence the +1 and −1 in the index.

The Figure Sup Mat 1 shows the main features of the model: to obtain similar division times with successive cell divisions (a linear increasing division time function) a strong inhibition is needed. On the other hand, almost simultaneous cells division (without any wave) is obtained by decreasing the amount of inhibition. To estimate parameters, we perform L_2 norm minimisation:

$$\chi^2(r,\rho,\mu,\delta) = \Sigma_{k=0}^{N} \left(T_k - t_k(r,\rho,\mu,\delta)\right)^2 \quad (3)$$

T_k are the division time for position $k \in \{..., -3, -2, -1, 0, 1, 2, 3,...\}$ from the $t_k$data and t_k (r, ρ, μ, δ) is the division time from the model with parameters r, ρ, μ, δ. We performed Nelder-Mead parameters optimisations in order to reach minimal χ^2. In order to obtain noisy representation, the algorithm performs 10 simulation of the differential equation with random starting values for A (uniform distribution between 0 and θ/2) except for the cell at position 0 which is set above threshold. The times of division are computed for each cell and the average is used as values t_k.

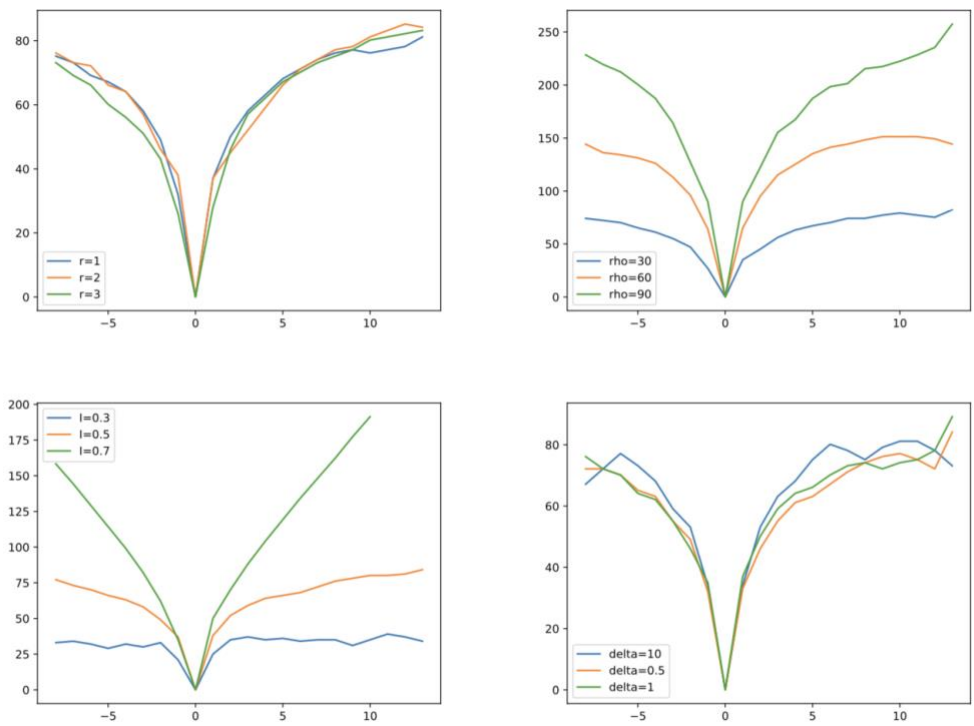

Figure Sup Mat 1. Top left. Simulation different production rate r ∈ {1, 2, 3} (other parameters are ρ = 30, μ = 0.5, δ = 1). Top right. Simulation with various temporal constant ρ ∈ {30, 60, 90} (other parameters are r = 2.1, μ = 0.5, δ = 1). This adjusts the temporal scale but not the shape of the wave. Bottom left. Simulation with various inhibition strength with μ ∈ {0.5, 0.6, 0.7} (other parameters are r = 2.1, ρ = 30, δ = 1). Strong inhibition here (0.7) imposes a more linear division time shape whereas low inhibition allows for quicker

division with neighbouring cells dividing almost simultaneously. Bottom right. Simulation with various inhibition time constant with $\delta \in \{10, 0.5, 1\}$ (other parameters are $r = 2.1$, $\rho = 30$, $\mu = 0.5$).

Supplementary figures

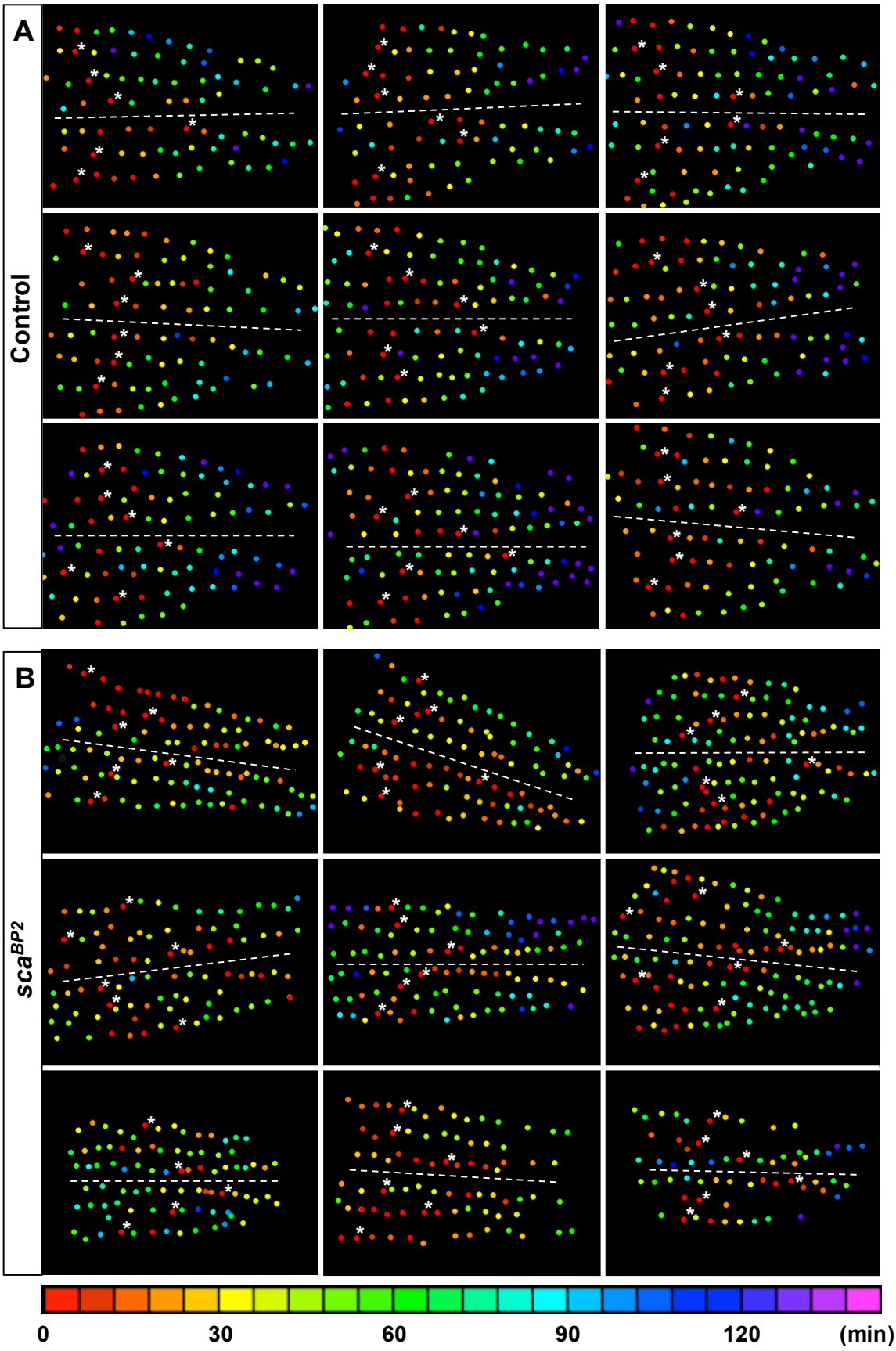

Figure S1. Illustrations of individual mitotic waves in control and *sca*^{BP2} mutant.

Heatmaps of nine nota showing the time of SOP division in control (A) and *sca*^{BP2} pupae (B). Circles represent SOP cells arranged in rows, anterior to the left. The relative time of division is colour coded according to the scale along the bottom, each colour covering 6 minutes. In each row, SOP_0 are marked by

white stars. Dashed lines show the midline. Note that in mutants, many cells are coloured in the reddish part of the spectra showing that several SOP cells divided simultaneously in the same row rather than in control where these cells are located in the anterior region of each row.

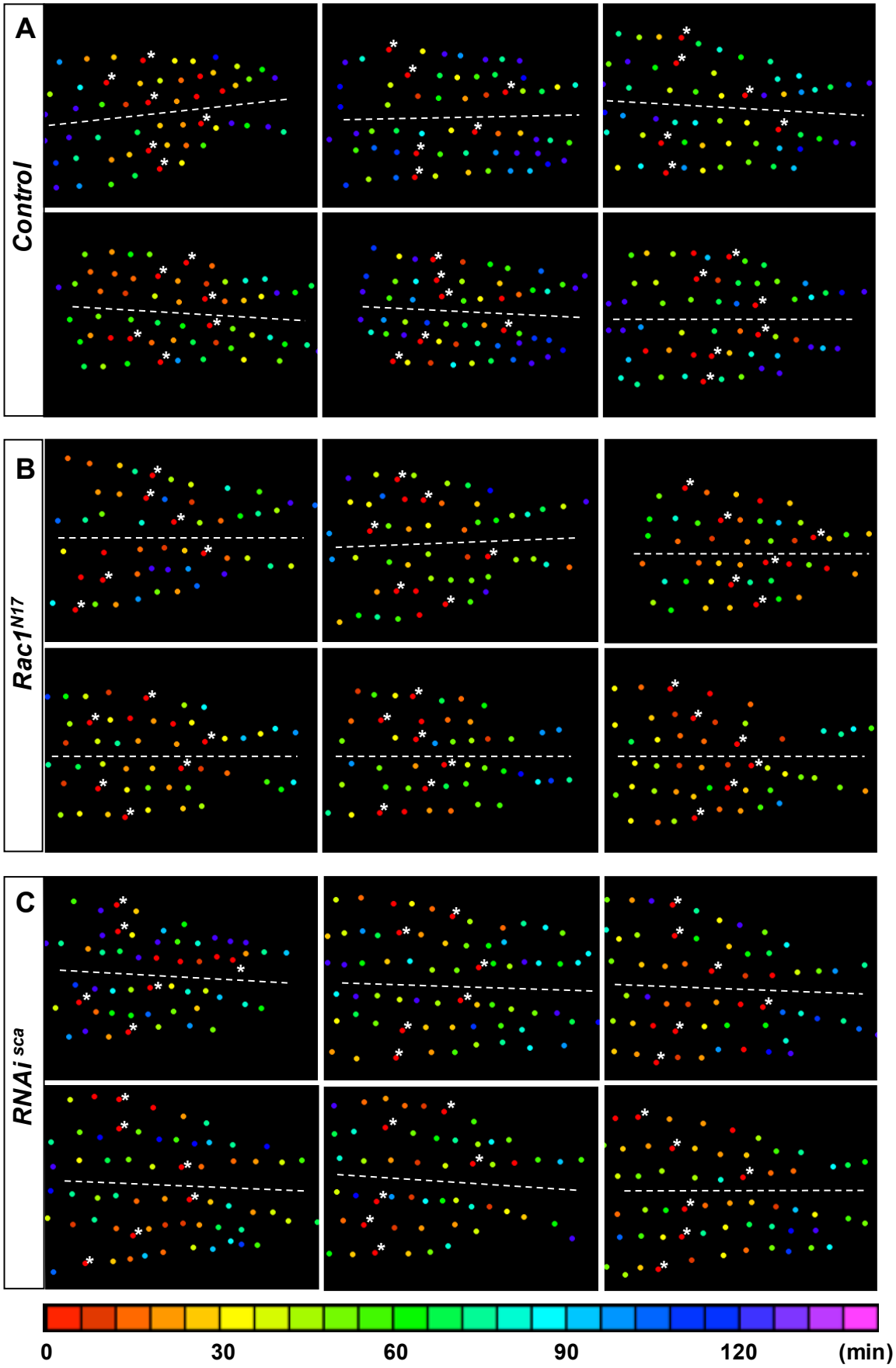

Figure S2. Illustrations of individual mitotic waves after reduction of cell protrusions by overexpression of Rac1^{N17} and after conditional inactivation of *sca*.

Heatmaps of six nota showing the time of SOP division in *neur>ph (PLCδ)::RFP/+; pnr>Gal4 tub> Gal80^{ts}/+* pupae (A), when cell protrusions were reduced in *neur>ph (PLCδ)::RFP/+; pnr>Gal4 tub> Gal80^{ts}/UAS-rac1^{N17}* pupae (B) and when *sca* was specifically downregulated between 12 and 19h APF,

starting just before and throughout the mitotic wave, using the conditional genetic context *pnr>gal4 tub GAl80^{ts} RNAi-sca* (C). Circles represent SOP cells arranged in rows, anterior to the left. The relative time of division is colour coded according to the scale along the bottom, each colour covering 6 minutes. In each row, SOP_0 are marked by white stars. Dashed lines show the midline. Note that in (B) and (C) that many cells are coloured in the reddish part of the spectra showing that several SOP cells divided simultaneously in the same row.

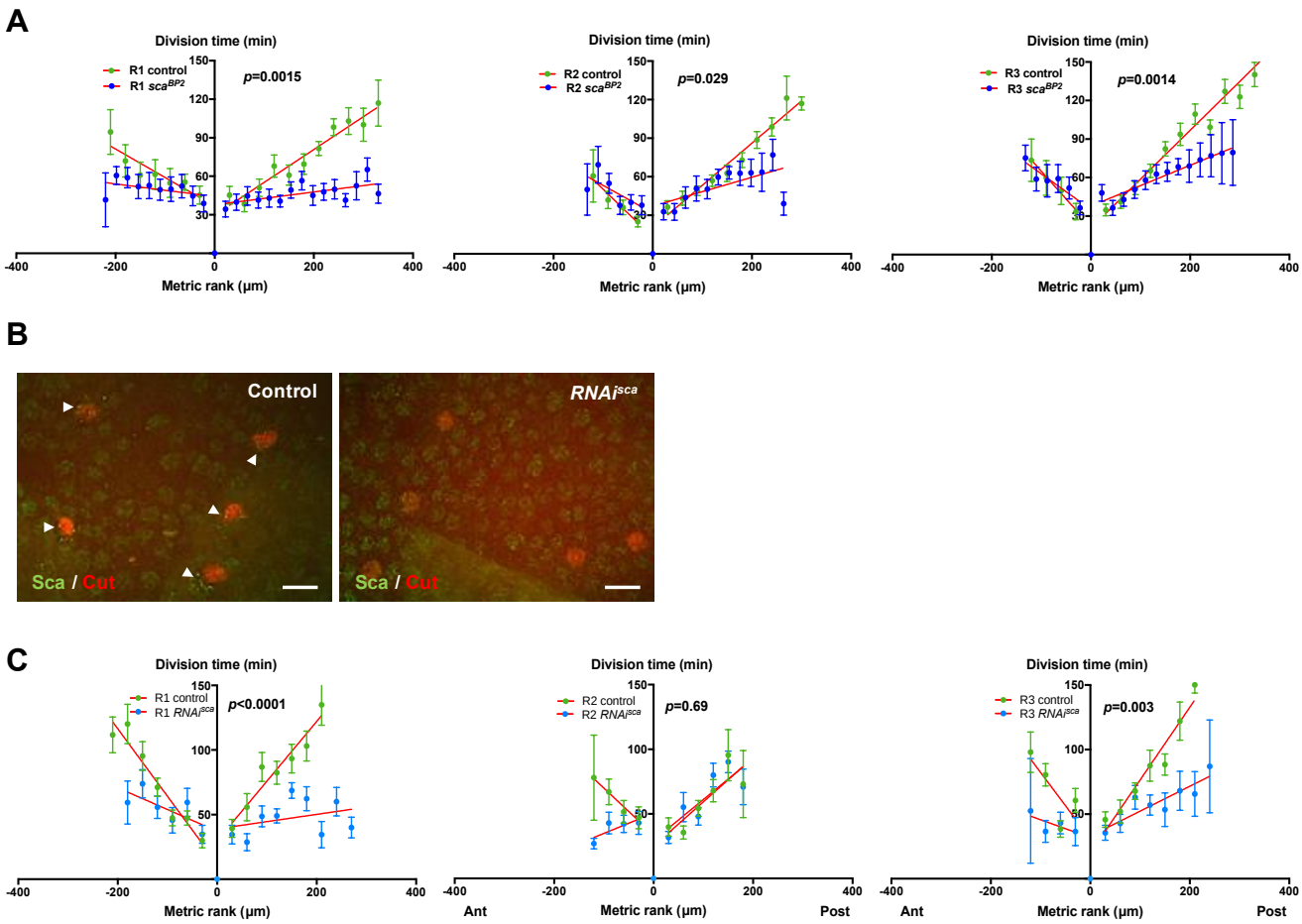

Figure S3. The amplitude of the mitotic wave is reduced in *sca* loss of function.

(A) The relative time of SOP cell division in control and *sca*^{BP2} homozygous mutant in row 1 (R1), row 2 (R2) and row 3 (R3) is plotted according to their relative position (mean time ± SEM, of 16 control nota and 9 *sca*^{BP2} nota). The position and the absolute time of division of SOP_0 in each row was taken as spatial and temporal references. The red lines correspond to standard linear regressions. (B) Efficiency of *RNAi-sca*. Immunostaining of Sca in control and after overexpression of *RNAi-sca* using the conditional genetic context *pnr>gal4 tub GAl80*^{ts} *RNAi-sca* in the protein trap sca::GFSTF. Note that Sca spots (green, arrowheads) in SOP cells, identified by Cut staining (red), disappear in *RNAi-sca* conditions. (C) The SOP mitotic wave in control and in flies where *sca* was specifically downregulated between 12 and 19h APF, starting just before and throughout the mitotic wave, using the conditional genetic context *pnr>gal4 tub GAl80*^{ts} *RNAi-sca* in row 1 (R1), row 2 (R2) and row 3 (R3). Mean time ± SEM of 10 control nota and 10 *RNAi-sca* nota. The position and the absolute time of division of the first cell which divided in each row was taken as spatial and temporal reference. Red lines correspond to standard linear regressions.

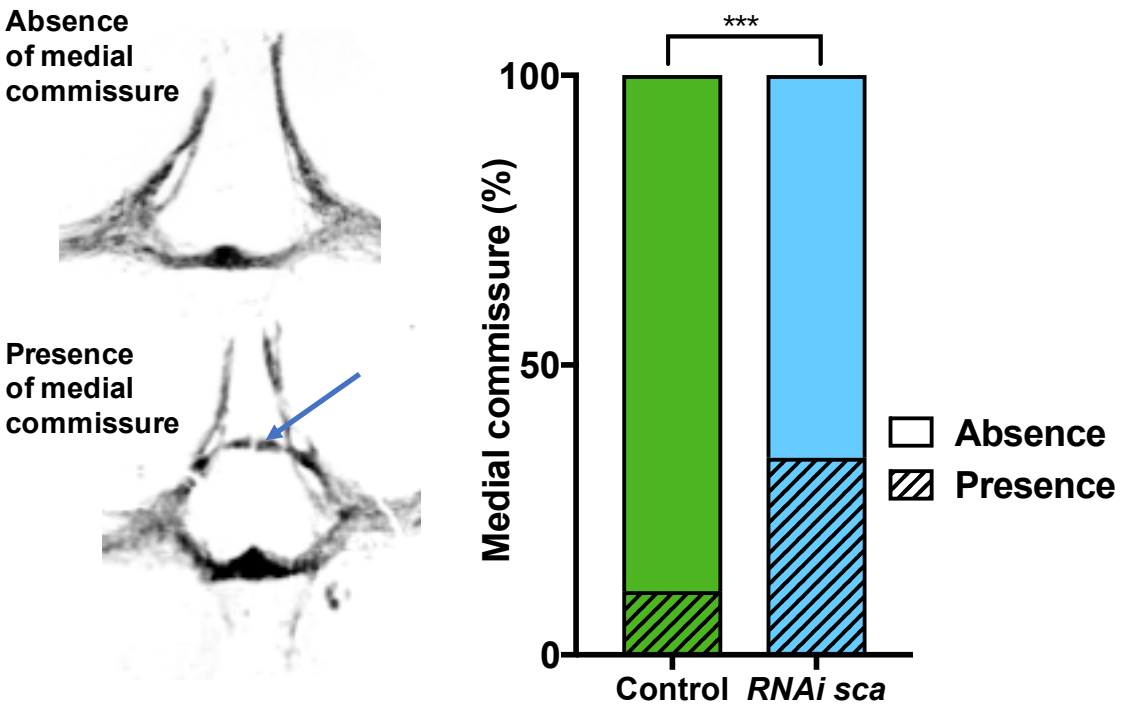

Figure S4. Sca downregulation modify the sensory neuropile structure.

On the left, the neuropile formed by all terminal axons from sensory organs on the central notum illustrating the absence (top) and presence (bottom) of the medial commissure in the thoracic ganglia (arrow). On the right, occurrence of the medial commissure in the thoracic ganglion of control and *RNAi-sca* flies; ***p = 0.0002, Fisher's exact test, control flies n = 64, *RNAi-sca* flies n = 63.

Key resource table

Reagent or resource	source	identifier	Additional information
Antibodies			
mouse anti-Futsch (clone 22C10)	DSHB	AB_528403	1/200
rabbit anti-HA (clone 3F10)	Roche	AB_231 4622	1/250
mouse anti-Flag (M2)	Sigma	AB_259529	1/250
anti-V5 (E10/V4RR), DyLight650	ThermoFisher	AB_2537642	1/100
anti-cut	DSHB	AB_528186	1/500
Fly strains			
w^{1118}	Bloomington Stock Center	BDSC_3605	
sca^{BP2}	Bloomington Stock Center	BDSC_7320	
UAS sca-RNAi	Vienna Drosophila Resource Center	VDRC#44527	
sca::GFSTF	Bloomington Stock Center	BDSC_64443	
neur>ph (PLCd)::RFP	Schweisguth F.		
UAS-MCFO-1	Bloomington Stock Center	BDSC_64085	
UAS-rac1^{N17}		BDSC_6292	
Dl^{7}		BDSC_485	
UAS-ph::GFP	Bellaiche Y.		
neur^{p72}*>Gal4*	Bellaiche Y.		

Table S1. Linear regression data

Genotype	Control								
	Row 1		Row 2		Row 3		Rows 1-3 (pooled)		
Linear regression	Anterior	Posterior	Anterior	Posterior	Anterior	Posterior	Anterior	Posterior	Pool (ant+post)
Best-fit values ± SE									
Slope	-0,22 ± 0,046	0,284 ± 0,024	-0,37 ± 0,06	0,3283 ± 0,0225	-0,34 ± 0,15	0,3805 ± 0,0229	-0,2631 ± 0,04339	0,3221 ± 0,01241	**0,3183 ± 0,01341**
1/slope	-4,5	3,521	-2,7	3,046	-3	2,628	-3,801	3,105	3,142
Speed (µm/min)	4,5	3,521	2,7	3,046	3	2,628	3,801	3,105	**3,142**
R square	0,82	0,9342	0,95	0,9636	0,54	0,9649	0,8803	0,9854	0,9707
Equation	Y = -0,22*X + 37	Y = 0,284*X + 26,03	Y = -0,37*X + 13	Y = 0,3283*X + 20,51	Y = -0,34*X + 26	Y = 0,3805*X + 20,68	Y = -0,2631*X + 27,8	Y = 0,3221*X + 23,17	Y = 0,3183*X + 22,9

Genotype	***Rac1*** ^{N17}								
	Row 1		Row 2		Row 3		Rows 1-3 (pooled)		
Linear regression	Anterior	Posterior	Anterior	Posterior	Anterior	Posterior	Anterior	Posterior	Pool (ant+post)
Best-fit values ± SE									
Slope	-0,02748 ± 0,04033	0,1483 ± 0,03153	-0,04935 ± 0,04737	-0,05545 ± 0,03652	-0,1102 ± 0,03911	0,3235 ± 0,127	0,04807 ± 0,07199	0,1633 ± 0,03744	**0,1438 ± 0,03292**
1/slope	-36,4	6,741	-20,26	-18,03	-9,073	3,091	20,8	6,123	6,952
Speed (µm/min)	36,4	6,741	20,26	18,03	9,073	3,091	27,25	6,123	**6,952**
R square	0,104	0,7867	0,2134	0,4346	0,7988	0,1603	0,446	0,1252	0,7367
Equation	Y = -0,02748*X + 33,54	Y = 0,1483*X + 32,61	Y = -0,04935*X + 34,76	Y = -0,05545*X + 41,41	Y = -0,1102*X + 34,55	Y = 0,3235*X + 20,39	Y = 0,04807*X + 34,82	Y = 0,1633*X + 29,77	Y = 0,1438*X + 30,03

Genotype	***Sca*** ^{RNAi}								
	Row 1		Row 2		Row 3		Rows 1-3 (pooled)		
Linear regression	Anterior	Posterior	Anterior	Posterior	Anterior	Posterior	Anterior	Posterior	Pool (ant+post)
Best-fit values ± SE									
Slope	-0,1686 ± 0,08467	0,0561 ± 0,06099	0,1576 ± 0,09048	0,3172 ± 0,1109	-0,1383 ± 0,09706	0,1929 ± 0,04038			
1/slope	-5,932	17,83	6,346	3,152	-7,233	5,185			
Speed (µm/min)	5,932	17,83	6,346	3,152	7,233	5,185			
								na	
R square	0,4978	0,1078	0,6027	0,6716	0,5036	0,7917			
Equation	Y = -0,1686*X + 37,1	Y = 0,0561*X + 38,95	Y = 0,1576*X + 50,6	Y = 0,3172*X + 29,36	Y = -0,1383*X + 31,81	Y = 0,1929*X + 32,99			

Genotype	***sca*** ^{BP2}***/sca*** ^{BP2}								
	Row 1		Row 2		Row 3		Rows 1-3 (pooled)		
Linear regression	Anterior	Posterior	Anterior	Posterior	Anterior	Posterior	Anterior	Posterior	Pool (ant+post)
Best-fit values ± SE									
Slope	-0,04933 ± 0,03233	0,04986 ± 0,01626	-0,2155 ± 0,1066	0,1123 ± 0,04281	-0,2776 ± 0,06459	0,1587 ± 0,01431			
1/slope	-20,27	20,06	-4,641	8,902	-3,603	6,303			
Speed (µm/min)	20,27	20,06	4,641	8,902	3,603	6,303			
								na	
R square	0,2254	0,4197	0,5052	0,4078	0,8219	0,9179			
Equation	Y = -0,04933*X + 44,16	Y = 0,04986*X + 37,78	Y = -0,2155*X + 31,71	Y = 0,1123*X + 37,13	Y = -0,2776*X + 35,15	Y = 0,1587*X + 37,87			

Genotype	***Dl*** ^{7}***/+***		
	Row 1		
Linear regression	Anterior	Posterior	Pool (ant+post)
Best-fit values ± SE			
Slope	-0,1325 ± 0,03879	0,1448 ± 0,02417	0.1472 ± 0.02304
1/slope	-7,548	6,906	6,791
Speed (µm/min)	7,548	6,906	6,791
R square	0,5932	0,7995	0,8195
Equation	Y = -0,1325*X + 28,93	Y = 0,1448*X + 25	"Y = 0.1472*X + 25.93"

Genotype	***sca*** ^{BP2}***/+***		
	Row 1		
Linear regression	Anterior	Posterior	Pool (ant+post)
Best-fit values ± SE			
Slope	-0,2487 ± 0,05619	0,2285 ± 0,03891	0,2547 ± 0,02863
1/slope	-4,022	4,377	3,925
Speed (µm/min)	4,022	4,377	3,925
R square	0,1488	0,8312	0,9188
Equation	Y = -0,2487*X + 31,15	Y = 0,2285*X + 32,13	Y = 0,2547*X + 30,04

Genotype	***Dl*** ^{7}***/sca*** ^{BP2}		
	Row 1		
Linear regression	Anterior	Posterior	Pool (ant+post)
Best-fit values ± SE			
Slope	-0,01871 ± 0,01919	0,03806 ± 0,03443	0,02307 ± 0,01829
1/slope	-53,45	26,27	43,35
Speed (µm/min)	53,45	26,27	43,35
R square	0,9508	0,1325	0,1659
Equation	Y = -0,01871*X + 48,08	Y = 0,03806*X + 47,49	Y = 0,02307*X + 48,35

REFERENCES

Aradhya, R., Zmojdzian, M., Da Ponte, J.P., and Jagla, K. (2015). Muscle niche-driven Insulin-Notch-Myc cascade reactivates dormant Adult Muscle Precursors in Drosophila. ELife *4*.

Ayeni, J.O., Audibert, A., Fichelson, P., Srayko, M., Gho, M., and Campbell, S.D. (2016). G2 phase arrest prevents bristle progenitor self-renewal and synchronizes cell division with cell fate differentiation. Development *143*, 1160–1169.

Baker, N., Mlodzik, M., and Rubin, G. (1990). Spacing diffentiation in the developing Drosophila eye: A fibrinogen-related lateral inhibitor encoded by scabrous. Science *250*, 1370–1377.

Bellaïche, Y., Gho, M., Kaltschmidt, J.A., Brand, A.H., and Schweisguth, F. (2001). Frizzled regulates localization of cell-fate determinants and mitotic spindle rotation during asymmetric cell division. Nat. Cell Biol. *3*, 50–57.

Buffin, E., and Gho, M. (2010). Laser microdissection of sensory organ precursor cells of Drosophila microchaetes. PloS One *5*, e9285.

Buszczak, M., Inaba, M., and Yamashita, Y.M. (2016). Signaling by Cellular Protrusions: Keeping the Conversation Private. Trends Cell Biol. *26*, 526–534.

Chou, Y.-H., and Chien, C.-T. (2002). Scabrous Controls Ommatidial Rotation in the Drosophila Compound Eye. Dev. Cell *3*, 839–850.

Cohen, M., Georgiou, M., Stevenson, N.L., Miodownik, M., and Baum, B. (2010). Dynamic Filopodia Transmit Intermittent Delta-Notch Signaling to Drive Pattern Refinement during Lateral Inhibition. Dev. Cell *19*, 78–89.

Corfas, G., and Dudai, Y. (1989). Habituation and dishabituation of a cleaning reflex in normal and mutant Drosophila. J. Neurosci. *9*, 56–62.

Deng, W.-M., Althauser, C., and Ruohola-Baker, H. (2001). Notch-Delta signaling induces a transition from mitotic cell cycle to endocycle in Drosophila follicle cells. Development *128*, 4737–4746.

Fernandes, V.M., Chen, Z., Rossi, A.M., Zipfel, J., and Desplan, C. (2017). Glia relay differentiation cues to coordinate neuronal development in Drosophila. Science *357*, 886–891.

Fichelson, P., and Gho, M. (2004). Mother–daughter precursor cell fate transformation after Cdc2 down-regulation in the Drosophila bristle lineage. Dev. Biol. *276*, 367–377.

Gatto, G., Smith, K.M., Ross, S.E., and Goulding, M. (2019). Neuronal diversity in the somatosensory system: bridging the gap between cell type and function. Curr. Opin. Neurobiol. *56*, 167–174.

Gavish, A., Shwartz, A., Weizman, A., Schejter, E., Shilo, B.-Z., and Barkai, N. (2016). Periodic patterning of the Drosophila eye is stabilized by the diffusible activator Scabrous. Nat. Commun. *7*.

Gho, M., Bellaïche, Y., and Schweisguth, F. (1999). Revisiting the Drosophila microchaete lineage. Development *126*, 3573–3584.

Ghysen, A. (1980). The projection of sensory neurons in the central nervous system of Drosophila: Choice of the appropriate pathway. Dev. Biol. *78*, 521–541.

Hampel, S., McKellar, C.E., Simpson, J.H., and Seeds, A.M. (2017). Simultaneous activation of parallel sensory pathways promotes a grooming sequence in Drosophila. ELife *6*.

Hirata, T., and Iwai, L. (2019). Timing matters: A strategy for neurons to make diverse connections. Neurosci. Res. *138*, 79–83.

Holguera, I., and Desplan, C. (2018). Neuronal specification in space and time. Science *362*, 176–180.

Hunter, G.L., Hadjivasiliou, Z., Bonin, H., He, L., Perrimon, N., Charras, G., and Baum, B. (2016). Coordinated control of Notch/Delta signalling and cell cycle progression drives lateral inhibition-mediated tissue patterning. Development *143*, 2305–2310.

Kornberg, T.B., and Roy, S. (2014). Cytonemes as specialized signaling filopodia. Development *141*, 729–736.

Krejčí, A., Bernard, F., Housden, B.E., Collins, S., and Bray, S.J. (2009). Direct Response to Notch Activation: Signaling Crosstalk and Incoherent Logic. Sci. Signal. *2*, ra1–ra1.

Lee, E.-C., Yu, S.-Y., and Baker, N.E. (2000). The Scabrous protein can act as an extracellular antagonist of Notch signaling in the Drosophila wing. Curr. Biol. *10*, 931-S2.

Li, Y. (2003). Scabrous and Gp150 are endosomal proteins that regulate Notch activity. Development *130*, 2819–2827.

McCormick, L.E., and Gupton, S.L. (2020). Mechanistic advances in axon pathfinding. Curr. Opin. Cell Biol. *63*, 11–19.

Mok, L.-P., Qin, T., Bardot, B., LeComte, M., Homayouni, A., Ahimou, F., and Wesley, C. (2005). Delta activity independent of its activity as a ligand of Notch. BMC Dev. Biol. *5*, 6.

Muñoz-Soriano, V., Santos, D., Durupt, F.C., Casani, S., and Paricio, N. (2016). Scabrous overexpression in the eye affects R3/R4 cell fate specification and inhibits notch signaling: SCA Overexpression Affects R3/R4 Cell Specification. Dev. Dyn. *245*, 166–174.

Muskavitch, M.A. (1994). Delta-notch signaling and Drosophila cell fate choice. Dev. Biol. *166*, 415–430.

Nern, A., Pfeiffer, B.D., and Rubin, G.M. (2015). Optimized tools for multicolor stochastic labeling reveal diverse stereotyped cell arrangements in the fly visual system. Proc. Natl. Acad. Sci. *112*, E2967–E2976.

Otsuki, L., and Brand, A.H. (2018). Cell cycle heterogeneity directs the timing of neural stem cell activation from quiescence. Science *360*, 99–102.

Petrovic, M., and Hummel, T. (2008). Temporal identity in axonal target layer recognition. Nature *456*, 800–803.

Petruccelli, E., Feyder, M., Ledru, N., Jaques, Y., Anderson, E., and Kaun, K.R. (2018). Alcohol Activates Scabrous-Notch to Influence Associated Memories. Neuron *100*, 1209-1223.e4.

Phillis, R.W., Bramlage, A.T., Wotus, C., Whittaker, A., Gramates, L.S., Seppala, D., Farahanchi, F., Caruccio, P., and Murphey, R.K. (1993). Isolation of Mutations Affecting Neural Circuitry Required for Grooming Behaviorin Drosophila melanogaster. Genetics *133*, 581–592.

Powell, P.A., Wesley, C., Spencer, S., and Cagan, R.L. (2001). Scabrous complexes with Notch to mediate boundary formation. Nature *409*, 626–630.

Renaud, O., and Simpson, P. (2001). scabrous Modifies Epithelial Cell Adhesion and Extends the Range of Lateral Signalling during Development of the Spaced Bristle Pattern in Drosophila. Dev. Biol. *240*, 361–376.

Sato, M., and Saigo, K. (2000). Involvement of pannier and u-shaped in regulation of Decapentaplegic-dependent wingless expression in developing Drosophila notum. Mech. Dev. *93*, 127–138.

Sato, M., Kojima, T., Michiue, T., and Saigo, K. (1999). Bar homeobox genes are latitudinal prepattern genes in the developing Drosophila notum whose expression is regulated by the concerted functions of decapentaplegic and wingless. Development *126*, 1457–1466.

Schindelin, J., Arganda-Carreras, I., Frise, E., Kaynig, V., Longair, M., Pietzsch, T., Preibisch, S., Rueden, C., Saalfeld, S., Schmid, B., et al. (2012). Fiji: an open-source platform for biological-image analysis. Nat. Methods *9*, 676–682.

Seeds, A.M., Ravbar, P., Chung, P., Hampel, S., Midgley, F.M., Mensh, B.D., and Simpson, J.H. (2014). A suppression hierarchy among competing motor programs drives sequential grooming in Drosophila. ELife *3*, e02951.

Usui, K., and Kimura, K. (1993). Sequential emergence of the evenly spaced microchaetes on the notum of Drosophila. Rouxs Arch. Dev. Biol. *203*, 151–158.

Usui-Ishihara, A., and Simpson, P. (2005). Differences in sensory projections between macro- and microchaetes in Drosophilid flies. Dev. Biol. *277*, 170–183.

Vandervorst, P., and Ghysen, A. (1980). Genetic control of sensory connections in Drosophila. Nature *286*, 65–67.

Zhang, N., Guo, L., and Simpson, J.H. (2020). Spatial Comparisons of Mechanosensory Information Govern the Grooming Sequence in Drosophila. Curr. Biol. *30*, 988-1001.e4.